Ocean Sci. Discuss., 12, 2423–2454, 2015
www.ocean-sci-discuss.net/12/2423/2015/
doi:10.5194/osd-12-2423-2015

Ocean Science Discussions
Open Access
EGU

River bulge evolution and dynamics in a non-tidal sea – Daugava River plume in the Gulf of Riga, Baltic Sea

E. Soosaar, I. Maljutenko, R. Uiboupin, M. Skudra, and U. Raudsepp

Marine Systems Institute at Tallinn University of Technology, Tallinn, Estonia

Received: 1 September 2015 – Accepted: 25 September 2015 – Published: 21 October 2015

Correspondence to: E. Soosaar (edith.soosaar@msi.ttu.ee)

Published by Copernicus Publications on behalf of the European Geosciences Union.

Abstract

Satellite remote sensing imagery and numerical modelling were used for the study of river bulge evolution and dynamics in a non-tidal sea, the Gulf of Riga (GoR) in the Baltic Sea. Total suspended matter (TSM) images showed a clearly formed anti-cyclonically rotating river bulge from Daugava River discharge during the studied low wind period. In about 7–8 days the bulge grew up to 20 km in diameter, before being diluted. Bulge growth rate was estimated as $r_b \sim t^{0.31\pm0.23}$ ($R^2 = 0.87$). A high resolution (horizontal grid step of 125 m) General Estuarine Transport Model (GETM) was used for detailed description of the development of the river plume in the southern GoR over the period when satellite images were acquired. In the model simulation, the $r_b \sim t^{0.5\pm0.04}$ ($R^2 = 0.90$). Both the model simulation and the satellite images showed that river water was mainly contained in the bulge and there were numerous intrusions at the outer perimeter of the bulge. We made numerical sensitivity tests with actual bathymetry and measured river runoff without wind forcing: (1) having initial 3-dimensional density distribution, (2) using initially a homogeneous ambient density field. In the first case, the anti-cyclonic bulge did not develop within the course of the model simulation and coastal current was kept offshore due to ambient density-driven circulation. In the second case, the river plume developed steadily into an anti-cyclonically recirculating bulge and a coastal current. This showed a significant effect of the wind in the evolution of the river bulge, even if the wind speed was moderate (3–4 $m\,s^{-1}$). In the second case, $r_b \sim t^{0.28\pm0.01}$ ($R^2 = 0.98$). While previous studies conclude that mid-field bulge region is governed by balance between centrifugal, Coriolis and pressure gradient terms, our study showed that geostrophic balance is valid for the entire mid-field of the bulge. In addition, while there is discharge into the homogenous GoR in case of high inflow Rossby number, the river inflow might split into two jets, with strong mixing zone in-between, in the plume near field region.

OSD
12, 2423–2454, 2015

1 Introduction

River water entering a coastal ocean typically forms a buoyant plume with an expanding anti-cyclonically rotating bulge near the river mouth and a coastal current in the coastally trapped wave direction (Fong and Geyer, 2002). Coastal currents are favoured in the case of low-discharge conditions and downwelling winds, while bulge formation is favoured during high-discharge conditions and upwelling winds (Chant et al., 2008). The anti-cyclonically recirculating bulge is characteristic of the surface advective plume (Yankovsky and Chapman, 1997) being a prominent feature in rotating tank experiments and numerical simulations under ideal conditions (Avicola and Huq, 2003; Horner-Devine, 2006; Thomas and Linden, 2007). Approximately 25–70 % of river water is trapped in the bulge (Fong and Geyer, 2002).

Observational studies confirm that the bulge is a naturally occurring phenomenon with many rivers (Chant et al., 2008; Horner-Devine et al., 2008; Horner-Devine, 2009; Valente and da Silva, 2009; Saldias et al., 2012; Hopkins et al., 2013; Mendas et al., 2014; Pan et al., 2014; Fernández-Nóvoa et al., 2015), but an anti-cyclonic rotation inside a bulge is observed seldom (Kudela et al., 2010; Horner-Devine, 2009; Chant et al., 2008). Observations of the evolution of the bulge over a certain time period are almost non-existent, with the exception of the Niagara River plume (Horner-Devine et al., 2008) and the Tagus estuary plume (Valente and da Silva, 2009). However, both cases are without clear evidence of anti-cyclonic circulation within the bulge.

In natural conditions, the evolution of the bulge is affected by properties of the outflow (Yankovsky and Chapman, 1997; Avicola and Huq, 2003a), tides (Valente and da Silva, 2009), wind (Dzwonkowski and Yan, 2005; Whitney and Garvine, 2005) and the ambient coastal current (Fong and Geyer, 2002). Thus, the evolution of the structure and circulation inside the bulge is difficult to observe. Exploitation of optical satellite remote sensing has extended the possibilities of monitoring and understanding the river plume dynamics under various hydrological, morphological and hydrodynamical conditions. A number of existing papers provide composite maps, where plume location

OSD
12, 2423–2454, 2015

and structure is described in response to prevailing wind conditions. Neither evolution of the bulge nor anti-cyclonic circulation within it can be identified from the composite satellite remote sensing images. Although each river plume can be considered as specific, Horner-Devine et al. (2015) have summarized the dynamics of an anti-cyclonically rotating bulge, with special emphasis on the river water volume re-circulating within the bulge. In their study, with reference to Nof and Pichevin (2001), they summarize that with stronger anti-cyclonic circulation within the bulge, more water recirculates in the bulge.

The aim of the present paper is to provide additional evidence of a well-developed anti-cyclonically rotating river bulge, using consecutive optical remote sensing images from a non-tidal sea and to assess current theoretical understanding of river bulge internal structure and dynamics from the complementary numerical model simulation results. We focus on the evolution of an anti-cyclonically rotating bulge during one life-cycle, i.e. from its formation until its dilution with ambient water. The horizontal expansion of the bulge from remote sensing imagery and the reproduction by numerical simulation are compared with modelled undisturbed bulge development and existing theoretical knowledge. The bulge depth, volume of the river water trapped in the bulge and the movement of the bulge centre are evaluated from model experiments. The validity of gradient wind (or cyclostrophic) balance (see Eq. 2 below) is evaluated for specific time instants in the mid-field region of the plume.

The eastern sub-basin of the Baltic Sea, the Gulf of Riga (GoR), is used as the study area (Fig. 1a). The GoR is almost bowl-shaped, has brackish water and is semi-enclosed (connection with the Baltic Sea through the Irbe Strait, 25 m deep, minimum cross-section area 0.4 km^2 and through the Virtsu Strait which is 5 m deep, minimum cross-section area 0.04 km^2). Small tidal oscillation (O [0.01–0.1 m]; Keruss and Sennikovs, 1999) allows us to consider it as a non-tidal estuary. The main freshwater source for the GoR is Daugava River in the south-east with a high discharge of 2500 $m^3 s^{-1}$ in early spring, which decreases to 200 $m^3 s^{-1}$ in late summer. The present

OSD
12, 2423–2454, 2015

study concentrates on the period from the last 12 days of March and early April 2007, when there was a high discharge of $\sim 2500\,m^3\,s^{-1}$ and low wind.

2 Materials and methods

2.1 Satellite data

ENVISAT/MERIS (Medium Resolution Imaging Spectrometer) data with 300 m resolution (from http://www.coastcolour.org/data/archive/) was used for monitoring bulge dynamics and structure. The MERIS images were processed using the Case-2 Regional algorithm (Doerffer and Schiller, 2007). We used total suspended matter (TSM) concentrations as a marker to distinguish turbid river water from "clear sea water", as TSM shows stronger contrast compared to other biological and physical parameters (SST, CHL etc). In studies performed by Siitam et al. (2014) and Attila et al. (2013), the reliability of the algorithm for TSM estimation in the coastal Baltic Sea was confirmed. An overall of seven sufficiently cloud free images were available from 20, 26, 27, 29, 30 March and 1 and 4 April. The images were acquired at about 9 a.m. UTC. The satellite data was interpolated to a regular 0.3 km × 0.3 km grid on the UTM-34v projection. Then the TSM concentrations were smoothed using a 3 × 3 point median filter.

2.2 River runoff and wind data

Daily volume flux for Daugava River was measured 35 km upstream from the river mouth (coordinates – 56.8516° N; 24.2728° E). Daily volume flux for Gauja and Lielupe rivers (see Fig. 1 for locations) was calculated from measured data. As locations of measurement stations are 55 and 95 km from the river mouth, the measured data was

OSD
12, 2423–2454, 2015

multiplied by factors 1.05 and 1.87 respectively[1], in order to obtain river discharge at the river mouth.

Wind data at one hour intervals was obtained from Ruhnu weather station, which is located on the Ruhnu Island in the central area of the Gulf of Riga (Figs. 1 and 2).

2.3 Numerical model setup: GETM

For numerical simulation we used the fully baroclinic and hydrostatic ocean model GETM (General Estuarine Transport Model, Burchard and Bolding, 2002) that is coupled to the GOTM (General Ocean Turbulence Model, Umlauf and Burchard, 2005) for vertical turbulence parameterization. The GETM uses a spherical coordinate system in the horizontal plane and a bottom-following vertical coordinate system. Using a mode splitting technique, GETM solves water dynamics on the Arakawa C-grid (Arakawa and Lamb, 1977). The GETM is characterized by advanced numerical techniques of advection schemes and internal pressure discretization schemes that minimize computational errors (Stips et al., 2004; Burchard and Rennau, 2008). In our setup we used the total variance diminishing (TVD) advection scheme for salinity, temperature and momentum (Pietrzak, 1998) and internal pressure parameterization suggested by Shchepetkin and McWilliams (2003). Advection scheme TVD P2-PDM was selected, as it has shown lower discrete variance decay rates than other widely used advection schemes (Pietrzak, 1998; Klingbeil, 2014).

The model domain covered the GoR with closed boundaries at the Irbe Strait and the Virtsu Strait. Topography was prepared using The Baltic Sea Bathymetry Database (BSHC 2013) and interpolated to a 125 m regular grid. Depths at the head of Daugava were adjusted to include Riga harbour fairway (depth 7 m). The vertical water column was split into 30 density adaptive layers, giving a vertical resolution of under 0.5 m (Gräwe et al., 2015). The barotropic time step was three seconds and the baroclinic

[1]Methodology worked out and in use for Gauja and Lielupe rivers in LVGMC – Latvian Environment, Geology and Meteorology Centre Institute, http://www.meteo.lv/en/.

OSD
12, 2423–2454, 2015

time step 60 s. Three rivers, Daugava, Lielupe and Gauja, were included. The meteorology was adopted from EMCWF ERA-Interim dataset (Dee at al., 2011)

The model simulation covered the period from 20 March to 5 April 2007. Initial salinity fields were interpolated from the 1 nautical mile simulation for the Baltic Sea (Maljutenko and Raudsepp, 2014). The density only depended on salinity. A 3 day spin-up period with a realistic salinity field and measured river run-off was used before including wind forcing on 20 March (real simulation). Initial TSM with zero initial concentration in the GoR and with unit concentration load from rivers was set as tracer variable.

3 Results

3.1 Satellite imagery

The first satellite image on 20 March showed the development of three river plumes. The Daugava River plume was far larger (about 8 km in diameter) than Gauja and Lielupe river plumes (Fig. 3a). From 17 to 20 March Daugava River discharge increased from 1500 to 2500 $m^3 s^{-1}$. The discharges of Lielupe and Gauja rivers were 230 and 180 $m^3 s^{-1}$ respectively. The river plumes were well distinguishable, as the ambient TSM concentrations was 2 $g m^{-3}$, compared to 20 $g m^{-3}$ in the bulge centre, in the southern part of the GoR. In all three cases, the river water had most likely initially spread offshore, then turned to the right and formed a coastal current. Thus, all three plumes consisted of a bulge area and a coastal current. Coastal current was detached from the coast, leaving a stripe of lower TSM water near the coast. Lielupe River plume was less pronounced than other river plumes, due to the blocking effect of the Daugava River plume on the right and the decline of the river discharge.

The wind conditions favoured the development of river plumes. From 15 to 19 March, wind speed increased from 2 to 10 $m s^{-1}$ (Fig. 2b), which could have generated sufficient mixing to destroy previously formed river plumes as well as avoided the develop-

OSD
12, 2423–2454, 2015

ment of a clearly distinguishable river plume. Just prior to the first satellite image, the wind speed dropped from 11 to 2 $m\,s^{-1}$, which may have considerably reduced wind mixing and enabled the free development of river plumes.

The next image was obtained on 26 March. The Daugava River bulge had grown significantly, to ~ 16 km in diameter (Fig. 3b). The core of the bulge was almost circular, with many intrusions along the outer rim. In the core of the bulge, freshly discharged water with high TSM concentration formed a jet with an anti-cyclonic spreading pattern along the left side of the bulge. The existence of coastal current could not be verified on the satellite image and the bulge manifested itself as more of a separate feature of the plume. Meanwhile the wind had been from the northeast, with a speed of 2–6 $m\,s^{-1}$ (Fig. 2b and c). This type of wind may have caused slight upwelling at the southeastern coast, downwind coastal currents over the shallow area and an offshore Ekman drift, resulting in the destruction of the coastal current and separation of the bulge. The Gauja River plume consisted of a bulge area and a coastal current attached to the coast. In the previous image, the coastal current of Gauja River plume had been slightly detached from the coast. The Lielupe River plume was almost undetectable, as the volume discharge had decreased to 130 $m^3\,s^{-1}$.

During the next 4 days, i.e. until 30 March, the wind speed was very low, between 0–2 $m\,s^{-1}$. We may assume that wind-driven currents and mixing were negligible. The Daugava River bulge remained almost circular and further detached from the coast. The main feature within the bulge was anti-cyclonically turning river water with high TSM concentration (Fig. 3c–e). This gives direct confirmation that water in natural buoyant bulges circulates anti-cyclonically in the Northern Hemisphere. More water intruded the southern GoR at the western boundary of the bulge. This intrusion spread anti-cyclonically, probably due to ambient circulation, and diluted with surrounding water. No clear coastal currents were visible.

By 1 April, the wind speed had increased to 4 $m\,s^{-1}$ and was blowing from the north. Daugava River discharge had reduced from ~ 2000 to ~ 1500 $m^3\,s^{-1}$ (Fig. 2). The image from 1 April still showed a circular bulge with a notably smaller TSM concentration

OSD
12, 2423–2454, 2015

than previously (Fig. 3f). The bulge had been transported westward and was nearly detached from the Daugava River outlet. The strong wind event of 10 m s^{-1} on 2 April had destroyed the bulge and river water with higher TSM concentration had smeared over the southern GoR by 4 April (Fig. 3 g).

3.2 Realistic simulation

The numerical model provides an opportunity for better and more detailed description of the development of the river plume in the southern GoR over the period when satellite images were acquired. The model considers TSM input only from the river discharges (no biology or resuspension from the sediments).

Daugava bulge had developed by 20 March in the numerical model (Fig. 3h). In the bulge, current velocities were up to 50 cm s^{-1} while ambient currents were about 5 cm s^{-1}. Strong momentum input by rivers caused spreading of tracers away from the coast, which matched the SPM pattern on the satellite image. In the case of the Daugava River plume, coastal counter-current blocked the spreading of tracers at the coast and the formation of a classical coastal current of the river plume. The offshore location of the maximum currents parallel to the coast and counter-current at the coast were remnants of the previous spreading of river water together with wind- and density-driven currents in the GoR.

By 26 March, bulge has not expanded as much as would be expected (Fig. 3i) based on satellite images from 20 and 26 March (Fig. 3a and b). In addition to strong momentum input from Daugava River, where current velocities were up to 30 cm s^{-1} in the bulge, the strong background anti-cyclonic circulation of about 20 cm s^{-1} prevailed over the south-eastern GoR. This circulation had pushed previous river water offshore and supported northward intrusion of bulge water. The coastal current had formed as a narrow band pressed against the coast. Bulge orientation, offshore extent, northward intrusion at the northern rim and south-westward intrusion at the south-western rim of the bulge were qualitatively comparable to similar features on the satellite image. Checking the sequence of tracer spreading in the numerical model showed that the

OSD
12, 2423–2454, 2015

plume on 26 March was the result of the reset of river plume on 24 March. The winds of 6 m s^{-1} from the northeast had hampered the free development of the river plume by mixing river water and transporting it offshore. Further developments of the Daugava River plume and especially the bulge until 30 March were quite consistent in the model and on the satellite images (Fig. 3i–l). Well-established anti-cyclonic circulation in the bulge, with a characteristic current speed of 20 cm s^{-1}, was confirmed in the model results. The numerical model captured the tendency of westward transport of the bulge from 30 March to 1 April. The bulge retained a circular shape on the satellite image, but was more distorted in the model (Fig. 3l and m). The numerical model showed that the regular river plume started to distort on 31 March (Fig. 3n). The strong wind event of 6–10 m s^{-1} on 2 April started to destroy the bulge in the model as well (Fig. 2).

3.3 Idealized simulations

In the realistic model simulation, the Daugava River plume was affected by river discharge, ambient currents and wind-driven currents. We made numerical sensitivity tests with (1) river discharge into a stratified GoR, while wind forcing was switched off, (2) river discharge into a homogeneous GoR with an ambient water salinity of 6 g kg^{-1}, while wind forcing was switched off (ideal simulation). In the first case, the anti-cyclonic bulge did not develop within the course of the model simulation and the coastal current was kept offshore due to ambient circulation (Fig. 4a). In the ideal run, river plume developed steadily into an anti-cyclonically recirculating bulge and a coastal current (Fig. 4b). The bulge length (offshore extent) and width (along-shore extent) as well as the width of the coastal current increased steadily in the course of the model simulation. Thus, comparison of the real run with test cases showed a significant effect of wind in the evolution of the river bulge, even if wind speed was moderate (see Fig. 2b).

OSD
12, 2423–2454, 2015

3.4 Temporal evolution of the bulge

The evolution of the river bulge is classically described by the spreading of the offshore front of the bulge and an increase of bulge depth (e.g. Avicola and Huq, 2003; Horner-Devine, 2006). There are uncertainties in the determination of the edges of a bulge as well as the volume of a bulge. In natural conditions, diffusion and mixing at the edges dilutes river water with surrounding water (Horner-Devine et al., 2015). We used TSM concentration to define the bulge boundary. On the satellite images, the threshold values were selected after a visual inspection of TSM concentration maps. Horner-Devine et al. (2008) have used a threshold value of normalized water-leaving radiance (nLw) in the 555 nm band to define the edges of the Niagara River plume on SeaWIFS satellite images. Our main criterion was to capture the circular part of the bulge and neglect coastal current as well as most of the intrusions. The threshold concentration varied from image to image as: (1) the TSM concentration of river water was variable and unknown for us, (2) locally, TSM concentration may have changed due to biological activity. The threshold value of $\log_{10}$ (TSM) was 1.0 for the image on 20 March, 1.2 for the images on 26, 27, 29 and 30 March and 1.1 for the image on 1 April. No bulge was defined for the image on 4 April. We checked the option to define the edges of the bulge, using spatial gradients of the TSM concentrations. Firstly, this approach did not eliminate the uncertainties, as the local maximum gradient isolines were discontinuous. Secondly, the boundaries of the bulge did not differ significantly from the boundaries that were determined using a threshold value for TSM concentration. In the numerical model, the bulge boundary was defined where $I = \log_{10}(\mathrm{TSM}) > -0.15$. We compared the temporal evolution of mean depth, radius and volume of the real and the ideal bulge from the numerical model.

The bulge effective radius, r_b, was estimated through the area of the bulge, A_b, assuming a circular shape of the bulge

$$r_b = \left(\frac{A_b}{\pi}\right)^{\frac{1}{2}}. \quad (1)$$

OSD
12, 2423–2454, 2015

According to the criterion of the bulge definition, the bulge is defined after about 0.5T, where T is rotation period of the earth (Fig. 5a and b) and $T = 0 \equiv 24$ March 2007 05:00 UTC. Steady increase of the real bulge took place during seven rotation periods. Both mean depth and radius as well as the volume were larger for the real bulge than for the ideal bulge. We would like to note the pulsation of the actual bulge – when bulge diameter increased, bulge mean depth decreased and vice versa. The decrease of the bulge diameter was faster than the decrease of bulge mean depth during the dissipation phase, which started from 7T. Occasionally, bulge depth even increased. Thus, the water in the bulge was mixed deeper during the dissipation phase.

The volume of river water that went into the bulge increased relatively fast during the first two rotation periods (Fig. 5c). In the real case, almost 60 % of river water was trapped inside the bulge, while in the ideal case the volume reached 45 %. We estimated the volume that was transported away by the coastal current. In order to be consistent with our bulge definition, we calculated water flow at the transect through the model grid cells where $I > -0.15$. During 2T, a negligible amount of river water was transported by the coastal current. During 2T the fraction of river water inside the bulge decreased monotonically, while the volume of coastal current increased (not shown). In the real case, water volume in the bulge increased until the bulge started to dissipate, but steadily retained its 50 % river water content. The fraction of river water started to increase from 4T, but did not exceed 5 % until the end of the simulation. In the case of the real bulge, our estimations showed that about 50 % of river water could be determined as either coastal current or as bulge due to intrusions and mixing at the boundaries of the bulge and the coastal current (see Fig. 3), unless we broaden the definition of the bulge. Still, it is obvious from satellite images and simulation results that a far larger amount of river water stayed within the bulge and was transported offshore by intrusions than the amount that formed a coastal current. In the ideal bulge, the fraction of river water decreased after 2T, while the coastal current increased. During 11T, the fraction of volume in the bulge and in the coastal current equilibrated. Thus,

OSD
12, 2423–2454, 2015

we may conclude that in the present case of the Daugava River plume, density- and wind-driven currents oppose the development of the coastal current.

3.5 Bulge momentum balance

The dynamics of the river bulge are described as balance between centrifugal, Coriolis and pressure gradient terms:

$$\frac{v_\theta^2}{r} + f v_\theta = g' \frac{\partial h}{\partial r} \tag{2}$$

as hypothesized by Yankovsky and Chapman (1997) and confirmed by Horner-Devine (2009) for the Columbia River plume. In Eq. (2), the v_θ is depth averaged angular velocity, r is radial distance from the bulge centre, f is Coriolis' parameter, g' is reduced gravity and h is bulge thickness. Left side of the equations is centrifugal ($T1$) and Coriolis term ($T2$) respectively, right side of the equation is pressure gradient term ($T3$). We calculated these terms for the case of the real bulge and the ideal bulge development on 29 March 2007 at 20:00 UTC (Fig. 6). As was the case previously, the bulge was defined where $I > -0.15$. The currents were strongest at the steepest slope of the bulge (Fig. 6a and b). Although the ideal and real bulges were similar quantitatively, the bulge centre was much closer to the coast (3 km) for the ideal bulge than for the real bulge (6 km). The outer thin area of the ideal bulge was wider than in the case of the real bulge. All terms in Eq. (2) showed higher absolute values at the steepest slope of the bulge (Fig. 6c–h). With the exception of the near field region, the centrifugal force was nearly an order of magnitude smaller than the Coriolis' term and the pressure gradient term. Geostrophic balance was valid for the entire mid-field of the bulge (Fig. 6 m and n). Taking into account the balance, Eq. (2), the error even increased slightly (Fig. 6o and p).

OSD
12, 2423–2454, 2015

3.6 Non-dimensional bulge spreading

The bulge radius was non-dimensionalized with the bulge Rossby radius

$$L_b = \left(\frac{2Qg'}{f^3}\right)^{\frac{1}{4}} \quad (3)$$

where Q is river runoff. In our case, the bulge Rossby radius varied between 2.7 and 3.1 km in time, according to the actual runoff of the Daugava River. Time series of increase of non-dimensional bulge radius from satellite images and the respective numerical simulations are presented in Fig. 7. We approximated the growth rate of the bulge radius using a power function. In the real case, we excluded the time period when the bulge started to dissipate, i.e. keeping the values until $8T$. The satellite remote sensing and the ideal simulation gave $r_b \sim t^{0.31\pm0.23}$ and $r_b \sim t^{0.28\pm0.01}$, with the coefficient of determination being $R^2 = 0.87$ and $R^2 = 0.98$, respectively. In the real simulation, $r_b \sim t^{0.50\pm0.04}$ ($R^2 = 0.90$). Thus, in the real model simulation, the growth of bulge radius was faster than in the ideal simulation. Using the thermal wind balance, Avicola and Huq (2003) estimated the growth rate of the bulge radius $r_b \sim t^{1/4}$, although in the laboratory experiments they obtained the growth rate $r_b \sim t^{2/5}$. From laboratory experiments, Horner-Devine et al. (2006) estimated that a buoyant surface advective bulge expands radially as $\sim t^{1/4}$ during the first 5 rotation periods and as $\sim t^{2/5}$ at later times. The measurement study for the Niagara River bulge (Horner-Devine et al., 2008) gave $\sim t^{0.46\pm0.29}$.

4 Discussion

A prominent feature in the satellite images and the model simulations was a well-developed anti-cyclonic circulation in the river bulge, which persisted for about 7–8 days. High river discharge and low wind conditions enabled undisturbed development

OSD
12, 2423–2454, 2015

of the bulge. The ideal model simulation showed that the bulge continued to develop steadily for at least 10 rotation periods. Horner-Devine (2006) argues that in the case of high inflow, i.e. large Froude number, $\mathrm{Fr} = U\left(g'H\right)^{-1/2}$, where $U = Q(HW)^{-1}$, W is river width and H is river depth, the plume becomes unstable after 5–6 rotation periods. In our case, the Froude number stayed between 0.9 and 1.5 during the whole modelling period (W = 700 m, H = 7 m). The plume was also stable in the numerical experiments of Nof and Pichevin (2001) and Fong and Geyer (2002).

We estimated the movement of the bulge centre in the ideal simulation. The bulge centre moved steadily to the north, completing about 8 km during nine rotation periods (Fig. 8a). As the centre also moved downstream actual offshore reach of the centre was 6 km. The radius of the ideal bulge increased from 4 to 9 km from 0.5T to 10T. Thus, by the end of our simulation the ratio of bulge centre, y_c, to bulge radius was less than 0.7, which according to Horner-Devine (2006) means that the bulge does not separate from the wall and flow into the coastal current does not decrease. The latter was evident from our numerical simulation with the ideal bulge.

The movement of the real bulge centre was more "chaotic" (Fig. 8b). At each one-hour timestep, the bulge centre was defined if the anti-cyclonic circulation with closed streamlines existed (i.e. Fig. 3k). When ambient current overrode bulge circulation, the bulge centre was not defined (i.e. Fig. 3i), although the bulge still existed if we look at the distribution of the tracer concentration. Thus, the movement of the bulge centre was not followed continuously. The main feature in the movement of the bulge centre was offshore-onshore oscillations (Fig. 8b). This behaviour is somewhat similar to bulge pinch-off described by Horner-Devine (2006). Horner-Devine (2006) proposed the ratio of internal radius, $L_i = U/f$, to bulge Rossby radius, $L^* = L_i/L_b$, to estimate bulge behaviour. In the case of the Daugava discharge, that ratio was between 0.81–1.26, which corresponds to situations where the bulge is forced offshore relative to its radius (Horner-Devine, 2006; Fig. 17d-g). In the case of a high Froude number and/or low g' (in our case 0.045 m s^{-2}), the bulge becomes unstable and the flow to the coastal current is reduced (Horner-Devine, 2006). The behaviour of the Daugava river bulge

OSD
12, 2423–2454, 2015

from satellite images and the real numerical model simulation (Fig. 3) showed that river water was mainly contained in the bulge and there were numerous intrusions at the outer perimeter of the bulge, which is qualitatively similar to the bulge behaviour in the model simulation by Horner-Devine (2006, his Fig. 14).

Horner-Devine et al. (2015) summarise the results of the volume fraction going into a coastal current current relative to river discharge, depending on inflow Rossby number. A relatively high Rossby number O [1] implies that most freshwater stays in the bulge while a lower Rossby number would imply that there is less water going into the bulge and more into the coastal current. In the Daugava River outflow, the inflow Rossby number varied between 3.4 and 5.7, which suggests that almost all of the river water should have been trapped in the bulge. Our estimates from the numerical model calculation showed that the fraction of river water that formed a coastal current was up to ten times smaller than the amount of river water that remained in the bulge. In the ideal case, considerable volume went into the coastal current, although the Q, Fr, Ro and g' were the same for ideal and real model simulations.

The explanation of the discrepancy between the ideal bulge and laboratory experiments could be the different behaviour of the plume in a near-field region. In a near-field region, river flow has a lift off point in the location where river water detaches from the bottom and the upper layer Froude number is equal to one (Horner-Devine et al., 2015). At the lift off point, vertical velocities cause shoaling of the plume interface and acceleration of the upper layer flow at a more seaward region. This, in turn, increases the Froude number, resulting in intense vertical mixing. In our idealized numerical simulation, the lift off occurred at about 0.5 km from the river mouth (Fig. 6a). The most intensive mixing started at one km from the coast where tracer concentrations were below the limit of the bulge definition (white area in Fig. 6a and low tracer concentration in Fig. 4a). The intensive mixing suppressed horizontal flow and the current velocities were low right behind the intense mixing zone, while the current velocities were higher at the left and right side of the mixing zone (Fig. 6a). Thus, the intensive mixing zone created a barrier for the river water flow and splitted it into two jets. The

OSD
12, 2423–2454, 2015

jet on the right formed a rotating bulge. As the barrier altered the flow direction, the flow angle was notably smaller than 90°, resulting in a bulge centre located closer to the coast (Avicola and Huq, 2003b). The jet on the left remained on the outer edge of the bulge. Such a barrier region is not observed in laboratory simulations. Natural buoyant river plumes have a small vertical to horizontal aspect ratio, O [10^{-3}], where vertical turbulent flux of density is considered to be dominant over horizontal turbulent fluxes (Horner-Devine et al., 2015). For laboratory simulations, the aspect ratio is at least an order of magnitude smaller. Horizontal turbulence flux would be comparable in magnitude with vertical mixing and a sharply separated region of intense mixing is far less likely to form. In addition, in our numerical simulations, the Daugava River runoff was smeared over 5 horizontal grid points right at the coast, which enables a better resolution of the river plume in the near field than, for instance, achieved by Hetland (2005).

In the case of the realistic model simulation, wind mixing overpowered the local mixing, therefore avoiding creation of the barrier region. The density-driven background currents restricted the development of a plume coastal current and pushed the river bulge offshore. As a result, the bulge centre was further away from the coast (see Fig. 8b).

5 Conclusions

Satellite TSM images showed a clearly formed river bulge from the Daugava River discharge during the studied low wind period. Satellite images also confirmed anti-cyclonic rotation inside the bulge. The bulge grew up to 20 km in diameter before being diluted. A high-resolution numerical model simulation repeated the plume behaviour satisfactorily and enabled a detailed study of the bulge dynamics. While previous studies conclude that balance in Eq. (2) is valid for the bulge, our study showed that geostrophic balance is valid for the entire mid-field of the bulge. Comparison of realistic and ide-

OSD
12, 2423–2454, 2015

alized model simulations showed a significant effect of wind-driven and density-driven circulation in the evolution of the river bulge, even if the wind speed was moderate.

The bulge radius was non-dimensionalized with the bulge Rossby radius. The satellite remote sensing and ideal simulation with no wind and uniform ambient density gave the growth of the non-dimensional bulge radius as $r_b \sim t^{0.31\pm0.23}$ and $r_b \sim t^{0.28\pm0.01}$, with the coefficient of determination being $R^2 = 0.87$ and $R^2 = 0.98$ respectively. In the real model simulation (measured wind and realistic ambient density), the $r_b \sim t^{0.50\pm0.04}$ ($R^2 = 0.90$). The bulge spreading rates agree well with laboratory experiments ($\sim t^{1/4}$ by Horner-Devine, 2006) and fit in the margin of the Niagara River bulge study ($\sim t^{0.46\pm0.29}$ by Horner-Devine et al., 2008).

Mean depth and radius as well as the volume were larger for the realistic model bulge than for the idealized bulge. River bulge behaviour from satellite images and the real numerical model simulation showed that river water is mainly contained in the bulge and there were numerous intrusions at the outer perimeter of the bulge. The fraction of river water that formed a coastal current was up to ten times smaller than the amount of river water that remained in the bulge.

In the ideal simulation, considerable volume went into the coastal current, although the Q, Fr, Ro and g' were the same for ideal and real model simulations. The ideal numerical model simulation showed that in the case of high inflow Rossby number the river inflow might split into two jets in the plume near field region, with a strong mixing zone in-between. Although the ideal and real bulges were similar, the bulge centre was closer to the coast in the case of the ideal bulge than in the case of the real bulge.

Acknowledgements. Volume flux data for Gauja and Lielupe rivers were provided by state limited Liability Company "Latvian Environment, Geology and Meteorology Centre" in Riga, Latvia. Volume flux data for river Daugava was provided by "Latvenergo AS" (State joint stock Company that provides electricity for the country's citizens).

OSD
12, 2423–2454, 2015

References

Arakawa, A. and Lamb, V. R.: Computational design of the basic dynamical processes of the UCLA General Circulation Model, Methods in Computational Physics, 17, 173–263, 1977.

Attila, J., Koponen, S., Kallio, K., Lindfors, A., Kaitala, S., and Ylöstalo, P.: MERIS Case II water processor comparison on coastal sites of the northern Baltic Sea, Remote Sens. Environ., 128, 138–149, 2013.

Avicola, G. and Huq, P.: The characteristics of the recirculating bulge region in coastal buoyant outflows, J. Mar. Res., 61, 435–463, 2003.

Baltic Sea Hydrographic Commission: Baltic Sea Bathymetry Database version 0.9.3, available at: http://data.bshc.pro/ (last access: 28 February 2014), 2013

Burchard, H. and Bolding, K.: GETM – a General Estuarine Transport Model, Scientific Documentation, Technical Report EUR 20253 EN, European Commission, available at: www.getm.eu (last access: 14 October 2015), 2002.

Burchard, H. and Rennau, H.: Comparative quantification of physically and numerically induced mixing in ocean models, Ocean Model., 20, 293–311, 2008.

Chant, R. J., Wilkin, J., Zhang, W., Choi, B.-J., Hunter, E., Castelao, R., Glenn, S., Jurisa, J., Schofield, O., Houghton, R., Kohut, J., Frazer, T. K., and Moline, M. A.: Dispersal of the Hudson River plume in the New York Bight: synthesis of observational and numerical studies during LaTTE, Oceanography, 21, 148–161, 2008.

Dee, D. P., Uppala, S. M., Simmons, A. J., Berrisford, P., Poli, P., Kobayashi, S., Andrae, U., Balmaseda, M. A., Balsamo, G., Bauer, P., Bechtold, P., Beljaars, A. C. M., van de Berg, L., Bidlot, J., Bormann, N., Delsol, C., Dragani, R., Fuentes, M., Geer, A. J., Haimberger, L., Healy, S. B., Hersbach, H., Holm, E. V., Isaksen, L., Kallberg, P., Köhler, M., Matricardi, M., McNally, A. P., Monge-Sanz, B. M., Morcrette, J.-J., Park, B.-K., Peubey, C., de Rosnay, P., Tavolato, C., Thepaut, J.-N., and Vitart, F.: The ERA-Interim reanalysis: configuration and performance of the data assimilation system, Q. J. Roy. Meteor. Soc., 137, 553–597, 2011.

Doerffer, R. and Schiller, H.: The MERIS case 2 water algorithm, Int. J. Remote Sens., 28, 517–535, 2007.

Dzwonkowski, B. and Yan, X.: Tracking of a Chesapeake Bay estuarine outflow plume with satellite-based ocean color data, Cont. Shelf Res., 25, 1942–1958, 2005.

OSD
12, 2423–2454, 2015

Fernández-Nóvoa, D., Mendes, R., Decastro, M., Dias, J., Sánchez-Arcilla, A., and Gómez-Gesteira, M.: Analysis of the influence of river discharge and wind on the Ebro turbid plume using MODIS-Aqua and MODIS-Terra data, J. Marine Syst., 142, 40–46, 2015.
Fong, D. A. and Geyer, W. R.: The alongshore transport of freshwater in a surface-trapped river plume, J. Phys. Oceanogr., 32, 957–972, 2002.
Gräwe, U., Holtermann, P., Klingbeil, K., and Burchard, H.: Advantages of vertically adaptive coordinates in numerical models of stratified shelf seas, Ocean Model., 92, 56–68, 2015.
Hetland, R. D. and Signell, R. P.: Modelling coastal current transport in the Gulf of Maine, Deep-Sea Res. II, 52, 2430–2449, 2005.
Hopkins, J., Lucas, M., Dufau, C., Sutton, M., Stum, J., Lauret, O., and Channelliere, C.: Detection and variability of the Congo River plume from satellite derived sea surface temperature, salinity, ocean colour and sea level, Remote Sens. Environ., 139, 365–385, 2013.
Horner-Devine, A. R.: Velocity, density, and transport measurements in rotating, stratified flows, Exp. Fluids, 1–13, 2006.
Horner-Devine, A. R.: The bulge circulation in the Columbia River plume, Cont. Shelf Res., 29, 234–251, 2009.
Horner-Devine, A. R., Fong, D. A., and Monismith, S. G.: Evidence for the inherent unsteadiness of a river plume: satellite observations of the Niagara River discharge, Limnol. Oceanogr., 53, 2731–2737, 2008.
Horner-Devine, A., Hetland, R., and Macdonald, D.: Mixing and transport in coastal river plumes, Annu. Rev. Fluid Mech., 47, 569–594, 2015.
Keruss, M. and Sennikovs, J.: Determination of tides in Gulf of Riga and Baltic Sea, in: Proc. International Scientific Colloqium "Modelling of Material Processing", Riga, available at: http://www.modlab.lv/publications/1999/publ7.htm (last access: 14 October 2015), 28–29 May 1999.
Klingbeil, K., Mohammadi-Aragh, M., Gräwe, U., and Burchard, H.: Quantification of spurious dissipation and mixing discrete variance decay in a finite-volume frame-work, Ocean Model., 81, 49–64, 2014.
Kudela, R. M., Horner-Devine, A. R., Banas, N. S., Hickey, B. M., Peterson, T. D., Lessard, E. J., Frame, E., Bruland, K. W., Lohan, M., Jay, D. A., Peterson, J., Peterson, B., Kosro, M., Palacios, S., and Dever, E. P.: Multiple trophic levels fueled by recirculation in the Columbia River plume, Geophys. Res. Lett., 37, L18607, doi:10.1029/2010GL044342, 2010.

OSD
12, 2423–2454, 2015

Maljutenko, I. and Raudsepp, U.: Validation of GETM model simulated long-term salinity fields in the pathway of saltwater transport in response to the Major Baltic Inflows in the Baltic Sea, in: IEEE/OES Baltic International Symposium (BALTIC), Tallinn, Estonia, 23–31, 26–29 May 2014.

Mendes, R., Vaz, N., Fernández-Nóvoa, D., Silva, J., Decastro, M., Gómez-Gesteira, M., and Dias, J.: Observation of a turbid plume using MODIS imagery: the case of Douro estuary (Portugal), Remote Sens. Environ., 154, 127–138, 2014.

Nof, D. and Pichevin, T.: The ballooning of outflows, J. Phys. Oceanogr., 31, 3045–3058, 2001.

Pan, J., Gu, Y., and Wang, D.: Observations and numerical modeling of the Pearl River plume in summer season, J. Geophys. Res.-Oceans, 119, 2480–2500, 2014.

Pietrzak, J.: The use of TVD limiters for forward-in-time upstream-biased advection schemes in ocean modeling, Mon. Weather Rev., 126, 812–830, 1998.

Saldías, G., Sobarzo, M., Largier, J., Moffat, C., and Letelier, R.: Seasonal variability of turbid river plumes off central Chile based on high-resolution MODIS imagery, Remote Sens. Environ., 123, 220–233, 2012.

Shchepetkin, A. F. and McWilliams, J. C.: A method for computing horizontal pressuregradient force in an oceanic model with a nonaligned vertical coordinate, J. Geophys. Res., 108, 3090, doi:10.1029/2001JC001047, 2003.

Siitam, L., Sipelgas, L., and Uiboupin, R.: Analysis of natural background and dredging-induced changes in TSM concentration from MERIS images near commercial harbours in the Estonian coastal sea, Int. J. Remote Sens., 35, 6764–6780, 2014.

Stips, A., Bolding, K., Pohlmann, T., and Burchard, H.: Simulating the temporal and spatial dynamics of the North Sea using the new model GETM (general estuarine transport model, Ocean Dynam., 54, 266–283, 2004.

Thomas, P. J. and Linden, P. F.: Rotating gravity currents: small-scale and large-scale laboratory experiments and a geostrophic model, J. Fluid Mech., 578, 35–65, 2007.

Umlauf, L. and Burchard, H.: Second-order turbulence closure models for geophysical boundary layers, a review of recent work, Cont. Shelf Res., 2, 795–827, 2005.

Valente, A. and Silva, J.: On the observability of the fortnightly cycle of the Tagus estuary turbid plume using MODIS ocean colour images, J. Marine Syst., 75, 131–137, 2009.

Whitney, M. and Garvine, R.: Wind influence on a coastal buoyant outflow, J. Geophys. Res., 110, C03014, doi:10.1029/2003JC002261, 2005.

OSD
12, 2423–2454, 2015

Yankovsky, A. E. and Chapman, D. C.: A simple theory for the fate of buoyant coastal discharges, J. Phys. Oceanogr., 27, 1386–1401, 1997.

OSD
12, 2423–2454, 2015

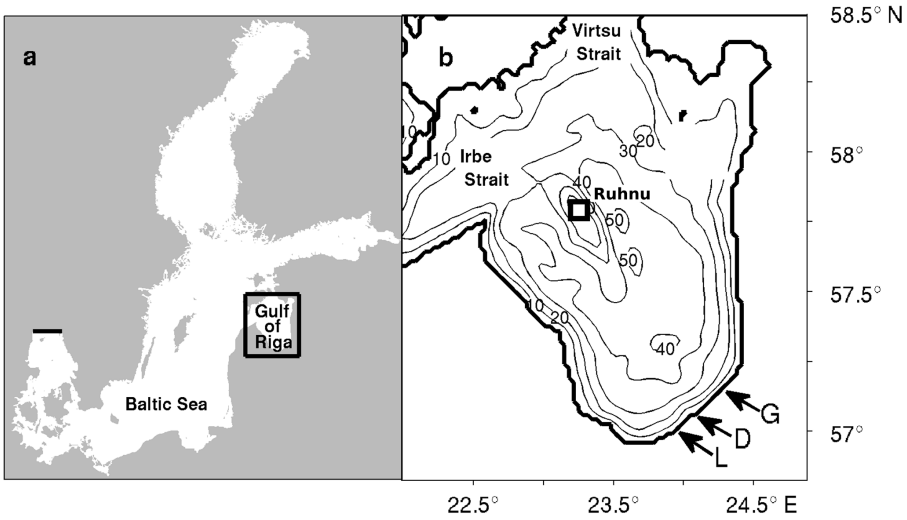

Figure 1. Map showing the location of the Gulf of Riga **(a)** and its topography **(b)**. Arrows mark river mouths locations for the Daugava (D), Lielupe (L) and Gauja (G) rivers. The square shows the location of the weather station.

OSD
12, 2423–2454, 2015

River bulge dynamics in a non-tidal sea

E. Soosaar et al.

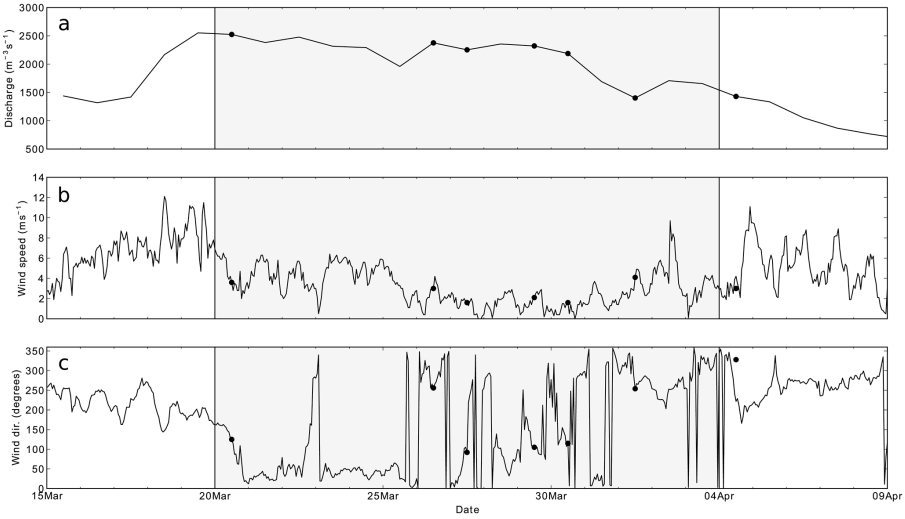

Figure 2. Time series of daily mean Daugava River discharge **(a)**, hourly wind speed **(b)** and wind direction **(c)** measured at Ruhnu weather station. Black dots show time instants when satellite images were acquired. The gray area marks the period between the first and last available satellite image from the study period (20 March to 4 April).

OSD
12, 2423–2454, 2015

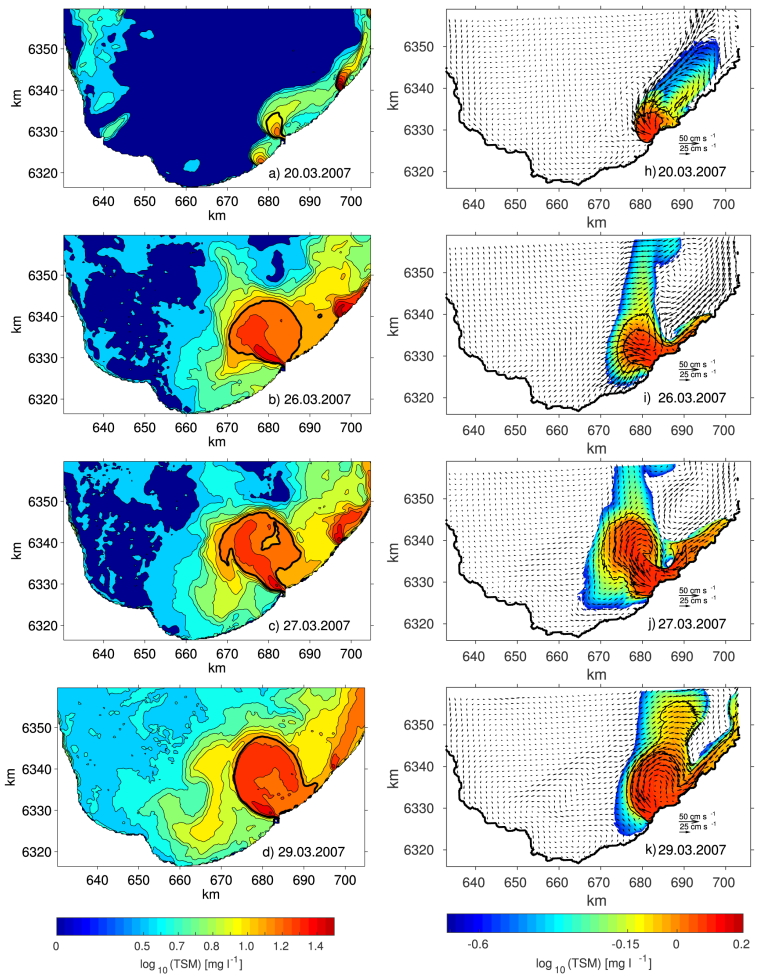

Figure 3.

OSD
12, 2423–2454, 2015

River bulge dynamics in a non-tidal sea

E. Soosaar et al.

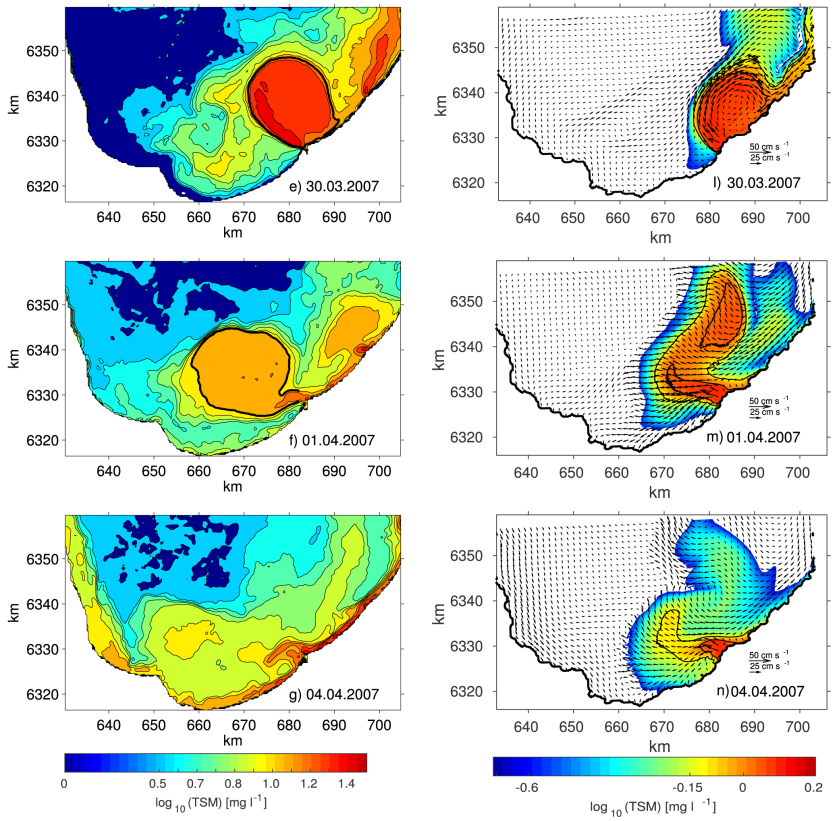

Figure 3. TSM concentration maps for the southern part of the Gulf of Riga from satellite images (left column) and TSM concentration and surface velocity maps from numerical simulation (right column). Bold contour on satellite images shows the edge of the Daugava River bulge. Black contours on the numerical model simulation maps represent TSM concentrations of $\log_{10}$ (TSM)= −0.15 and = −0.05. The former is used for the determination of the Daugava River bulge. The coordinate system is on the UTM-34v projection.

OSD
12, 2423–2454, 2015

River bulge dynamics in a non-tidal sea

E. Soosaar et al.

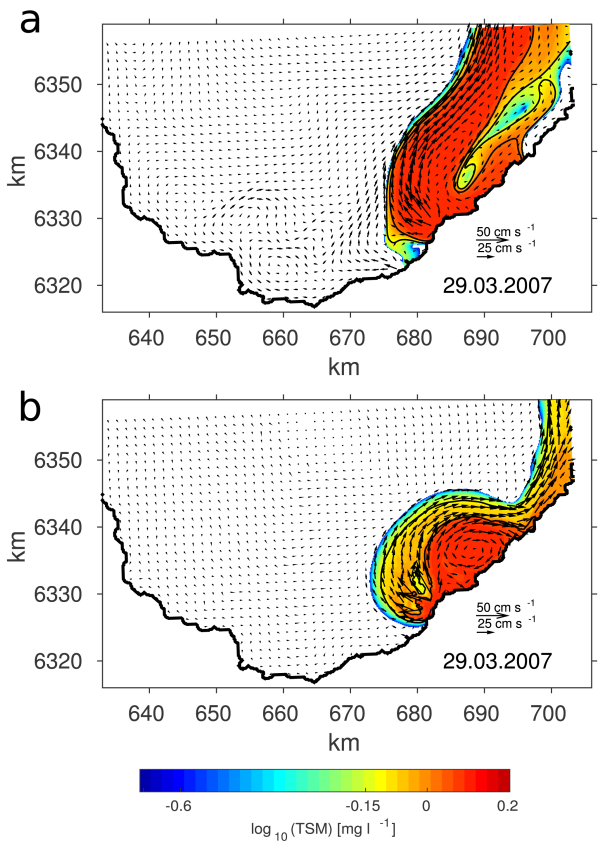

Figure 4. Instantaneous surface velocity and TSM concentration maps for simulation with realistic ambient density and no wind forcing **(a)** and idealized model simulation with uniform ambient density and no wind forcing **(b)** at 12:00 (UTC) on 29 March 2007. Solid lines represent TSM concentrations of $\log_{10}$ (TSM) = −0.15 and = −0.05. The coordinate system is on the UTM-34v projection.

OSD
12, 2423–2454, 2015

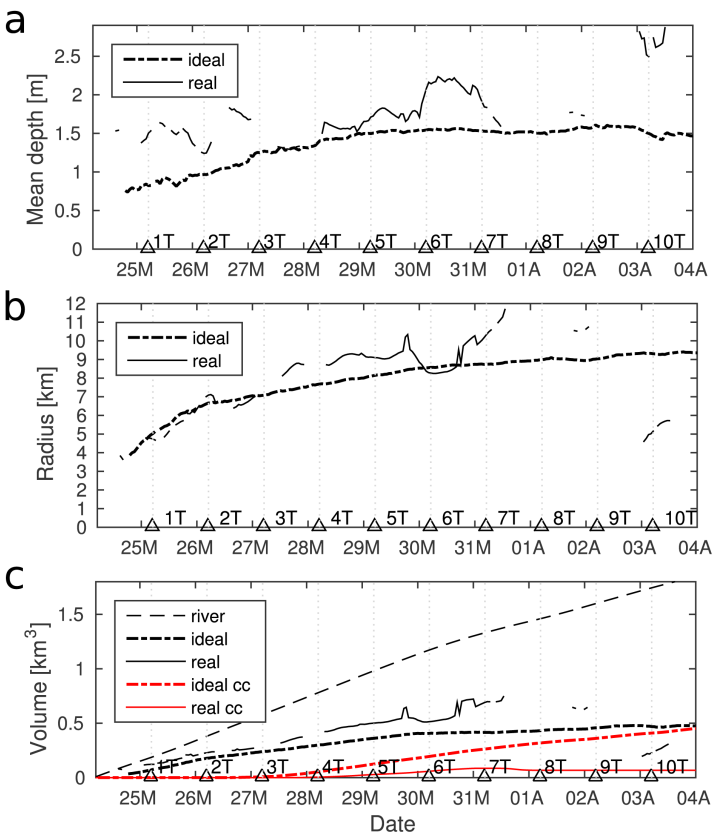

Figure 5. Time series of the Daugava River bulge mean depth **(a)** and bulge radius **(b)** and volume **(c)**. The solid line represents the real model simulation and dash-dotted line the idealized model simulation. Time series of cumulative river water (dashed), bulge volume (black) and volume of the coastal current (red) in the real model simulation (solid) and ideal model simulation (dash-dotted) **(c)**. Triangles represent the rotation period of the earth starting from 24 March 2007 05:00 UTC.

OSD
12, 2423–2454, 2015

River bulge dynamics in a non-tidal sea

E. Soosaar et al.

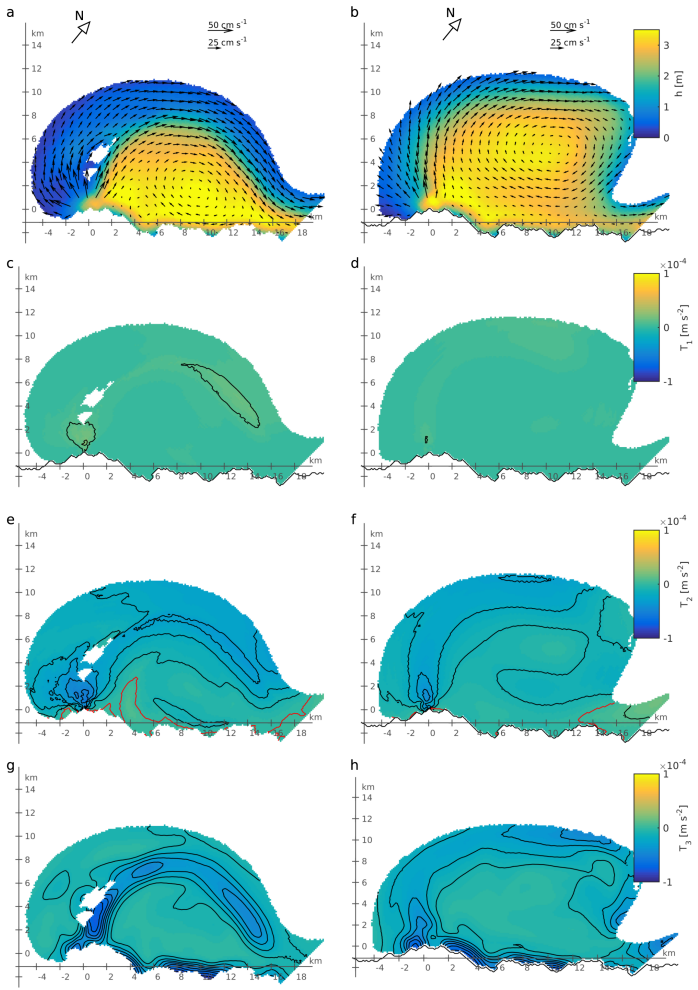

Figure 6.

OSD
12, 2423–2454, 2015

River bulge dynamics in a non-tidal sea

E. Soosaar et al.

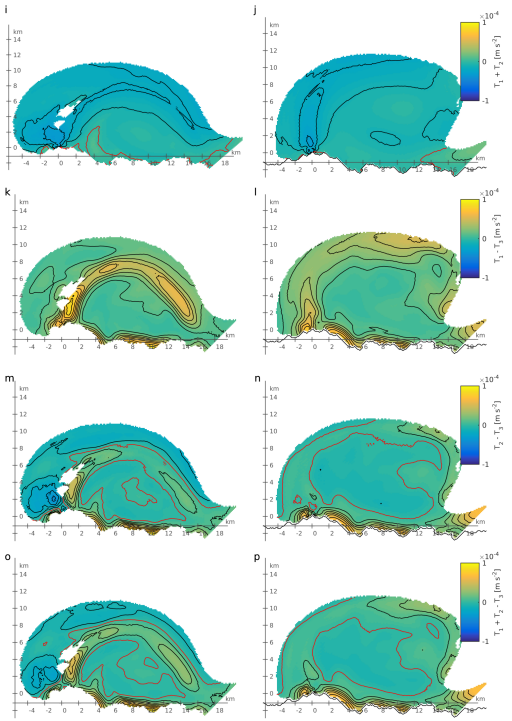

Figure 6. Bulge depth and depth averaged velocities, the terms (T_1, T_2, T_3) of the balance (see Eq. 2) and the combinations of the terms for idealized (left column) and realistic (right column) model simulations on 29 March 2007 at 20:00 UTC. Bulge depth and depth averaged velocities (**a** and **b**), centrifugal term (T_1) (**c** and **d**), Coriolis term (T_2) (**e** and **f**), pressure gradient term (T_3) (**g** and **h**), $T_1 + T_2$ (**i** and **j**), $T_1 - T_2$ (**k** and **l**), $T_2 - T_3$ (**m** and **n**) and $T_1 + T_2 - T_3$ (**o** and **p**). The contour interval is 1 m s^{-2}. The red isoline represents zero. The blank area within the bulge is where the tracer concentrations were below the threshold values of the bulge definition. The origin of the coordinate system is at the mouth of Daugava River. True north is shown by the arrow.

OSD
12, 2423–2454, 2015

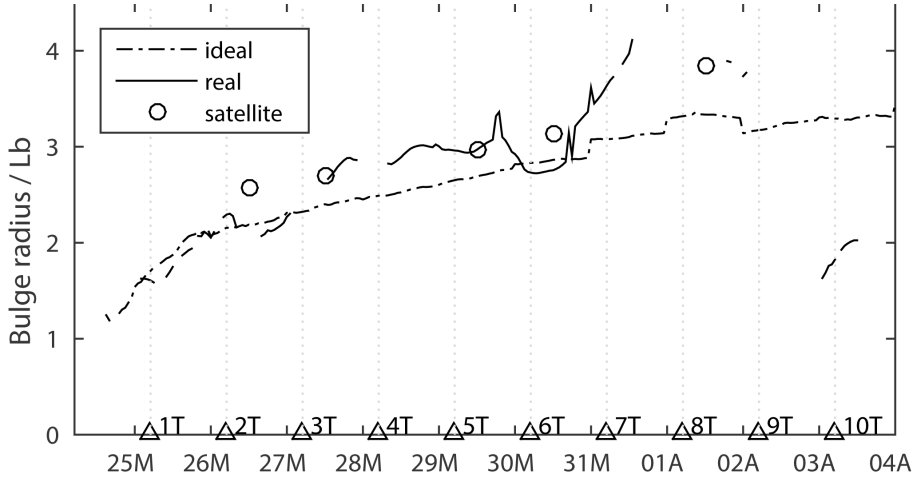

Figure 7. Time series of the bulge effective radius scaled with bulge Rossby radius from satellite data (circles), real (solid) and idealized (dash-dotted) numerical simulations. Triangles represent the rotation period of the earth starting from 24 March 2007 05:00 UTC.

OSD
12, 2423–2454, 2015

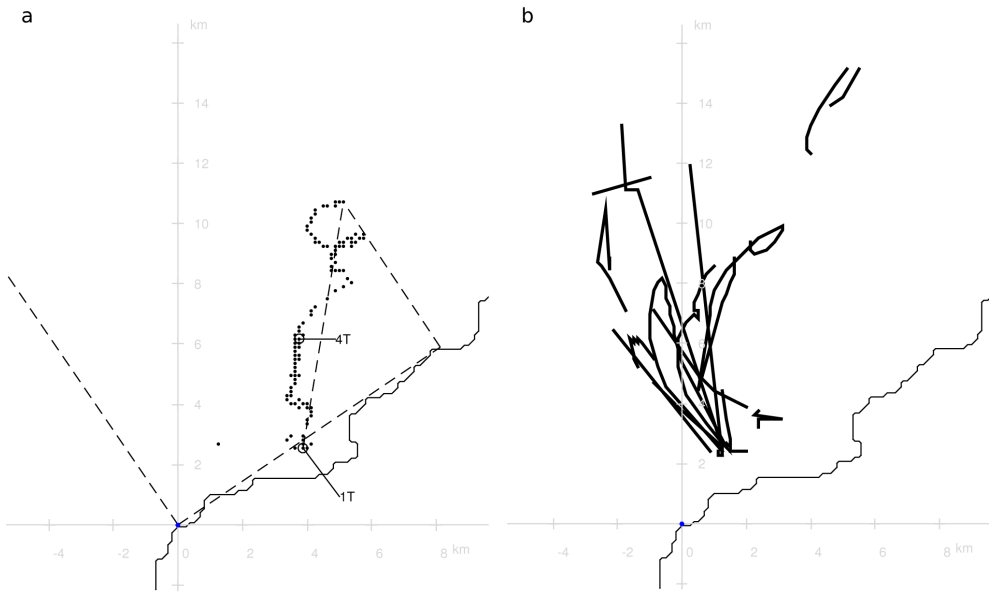

Figure 8. The trajectories of the bulge centre for the idealized simulation **(a)** and the realistic simulation **(b)** from 24 March 2007 05:00 to 5 April 2007 00:00 UTC. Each dot shows the location of the bulge centre at hourly intervals. Dashed lines show the normal and tangent to the coastline, distance of the bulge centre from the location at 1*T* to the end of the simulation, the distance of the bulge centre at the end of the simulation to the coast in the direction of the normal to the coast. 1*T* and 4*T* show the location of the bulge centre after one and four rotation periods of the earth starting from 24 March 2007 05:00 **(a)**. Discontinuities in the bulge trajectories for the realistic model simulation are because the bulge centre was defined only if anti-cyclonic circulation with closed streamlines existed **(b)**.

OSD
12, 2423–2454, 2015